Proceedings of the 16th Czech and Slovak Conference on Magnetism, Košice, Slovakia, June 13–17, 2016

Glass Forming Abilities and Crystallization Process in Amorphous Pr–Fe–Co–Zr–Nb–B Alloys of Various B Content

K. Pawlik[a], P. Pawlik[a,*], W. Kaszuwara[b] and J.J. Wysłocki[a]

[a]Institute of Physics, Częstochowa University of Technology, al. Armii Krajowej 19, 42-200 Częstochowa, Poland

[b]Faculty of Materials Science and Engineering, Warsaw University of Technology, Wołoska 141, 02-507 Warsaw, Poland

The influence of boron contents on the glass forming abilities and magnetic properties of melt-spun ribbon samples produced from $Pr_9Fe_{50+x}Co_{13}Zr_1Nb_4B_{23-x}$ (x = 0, 2, 5, 8) alloys, were investigated. For all compositions, the rapidly solidified samples were fully amorphous, which was confirmed by X-ray diffractometry and the Mössbauer spectroscopy. Differential scanning calorimetry and differential thermal analysis studies revealed good glass forming abilities for all investigated specimens and allowed to determine thermal stability parameters of the amorphous phase. For all alloy ribbons, very large supercooled liquid region before crystallization ΔT_x reaching 100 K was measured. The Kissinger plots were constructed to determine the activation energies for crystallization. Annealing of specimens at temperatures ranging from 923 K to 1033 K for 5 min resulted in significant change of the phase constitution. The X-ray diffractometry studies have shown presence of hard magnetic $Pr_2(Fe, Co)_{14}B$ and paramagnetic $Pr_{1+x}Fe_4B_4$ phases. Furthermore, with the increase of B contents in the alloy composition crystallization of α-Fe phase occurs at wider range of the annealing temperature. Anomaly of both thermal and magnetic properties was observed for the $Pr_9Fe_{52}Co_{13}Zr_1Nb_4B_{21}$ alloy ribbons.

DOI: 10.12693/APhysPolA.131.979

PACS/topics: 64.70.dg, 61.05.cp, 75.20.En, 75.50.Vv

1. Introduction

An important aspect that determines practical application of hard magnetic nanocrystalline alloys, is the tailoring of their technical parameters, such as the coercivity field ${}_JH_C$, remanence J_r and maximum magnetic energy product $(\boldsymbol{BH})_{\max}$. Rapid solidification leading to the amorphous structure allows obtaining appropriate nanocrystalline structure and hard magnetic properties by controlled annealing. Furthermore, high costs of commercialized RE–Fe–B (RE = rare earth) magnets drew attention to materials containing lower fraction of RE elements. A good example of such materials is $(Pr, Dy)_{4.5}(Fe, Co)_{73.5}Zr_1B_{20}$ alloy for which it was possible to cast bulk amorphous samples in the form of 1 mm diameter rods, and thin-walled tubes of outer diameters up to 3 mm [1]. However, low content of the hard magnetic phase precipitating during devitrification annealing of the amorphous phase, causes low values of ${}_JH_C \approx 180$ kA/m and $(\boldsymbol{BH})_{\max}$ of ≈ 47 kJ/m^3. In order to increase the fraction of hard magnetic phase extensive studies were carried out on RE–Fe–Co–B alloys, doped with Zr, Ti, C and Nb, containing 6–9 at.% of RE (where RE = Nd, Pr, Dy) [2–4]. It was possible to produce up to 4 mm diameter amorphous rods for the Nd–Fe–B alloy containing 6 at.% of Nd, doped with 4 at.% of Nb [5]. Increase of Nd content to $\approx$ 9.5 at.% was detrimental to the maximum size of amorphous samples (down to 1.5 mm diameter rods). However, annealing allowed to produce nanocrystalline magnets, for which the coercivity reached 1.1 MA/m, while $(\boldsymbol{BH})_{\max}$ of ≈ 33 kJ/m^3 was rather low. Our studies carried out on suction-cast plates suggested changes of the glass forming abilities in $Pr_9Fe_{50+x}Co_{13}Zr_1Nb_4B_{23-x}$ (x = 0, 2, 5, 8) alloys of various B contents [6]. The objective of the present work was determination of glass forming abilities and investigation of the influence of the B contents and annealing conditions on the phase constitution and magnetic properties of the $Pr_9Fe_{50+x}Co_{13}Zr_1Nb_4B_{23-x}$ (x = 0, 2, 5, 8) alloy ribbons.

2. Samples preparation and experimental methods

The ribbon samples of nominal compositions $Pr_9Fe_{50+x}Co_{13}Zr_1Nb_4B_{23-x}$ (x = 0, 2, 5, 8) were melt-spun at constant velocity of the copper roll surface of 25 m/s under argon atmosphere. Subsequently the specimens were annealed at temperatures ranging from 923 K to 1033 K for 5 min. Thermal stability parameters were determined using differential thermal analysis (DTA) and differential scanning calorimetry (DSC) techniques. To establish the activation energies for crystallization the DSC curves were measured in the temperature range 300–973 K with different heating rates 10 K/min $\leq \beta \leq$ 40 K/min for each alloy composition. The phase constitution was analyzed by X-ray diffractometry (XRD) with Cu K_α radiation. Furthermore, the crystallite sizes and weight fractions of constituent phases were calculated using the Rietveld refinement. Hysteresis loops were measured using LakeShore VSM magnetometer operating in external magnetic fields up to 2 T at room temperature.

*corresponding author; e-mail: pawlik@wip.pcz.pl

3. Results and discussion

The DSC scans measured with $\beta = 20$ K/min for the amorphous ribbon samples of all investigated compositions are presented in Fig. 1. These measurements allowed to determine the thermal stability parameters of the samples (Table I). For $x = 0$ and $x = 5$ alloys, two distinct exothermic peaks are observed on heat flow curves, however the second peak is not well pronounced. For the $x = 2$ alloy ribbon the highest crystallization temperature ($T_x = 956$ K) and the largest supercooled liquid region value ($\Delta T_x = 118$ K) were measured. It has also after effect in the phase constitution and magnetic properties of this ribbon subjected to annealing. For all studied samples significantly large supercooled liquid region before crystallization were measured, much higher than those for $Pr_{4.5-x}Dy_xFe_{61}Co_{13.5}Zr_1B_{20}$ ($x = 0$, 1) alloys [7]. According to [8] such large ΔT_x values are related to simultaneous crystallization of multiple phases.

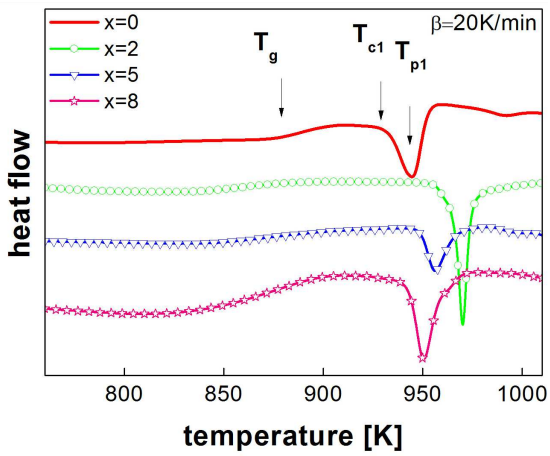

Fig. 1. DSC curves for $Pr_9Fe_{50+x}Co_{13}Zr_1Nb_4B_{23-x}$ ($x = 0$, 2, 5, 8) alloy ribbons.

TABLE I

Thermal stability parameters determined for amorphous ribbons of $Pr_9Fe_{50+x}Co_{13}Zr_1Nb_4B_{23-x}$ ($x = 0$, 2, 5, 8) alloys: T_g — glass transition temperature, T_x — onset crystallization temperature, T_p — crystallization peak temperature, $\Delta T_x = T_x - T_g$ — supercooled liquid region, E_a [kJ/mol] — activation energy.

x [at.%]	T_g [K]	T_x [K]	T_p [K]	ΔT_x [K]	E_a [kJ/mol]
0	875	931	944	56	397
2	838	956	969	118	498
5	846	948	955	102	456
8	830	942	948	112	420

The effective activation energies E_a for crystallization were determined from the Kissinger plots (Fig. 2). Values of E_a (Table I) are relatively high especially for $x = 2$ sample ($E_a = 498 \pm 26$ kJ/mol) indicating particularly stable amorphous state for this composition. DTA measurements were also performed in order to determine the melting temperatures (T_m), liquidus temperatures (T_l) and GFA parameters for the samples (Table II). The T_m as well as T_l for all alloys remain constant. Furthermore, in all cases similar values of the reduced glass transition temperature (defined as $T_{rg} = T_g/T_l$) $T_{rg} \approx 0.60$ were calculated. Glass forming ability parameter γ (defined as $\gamma = T_x/(T_l + T_g)$) reached the highest value of 0.425 for $x = 2$ alloy suggesting best GFA among studied alloys.

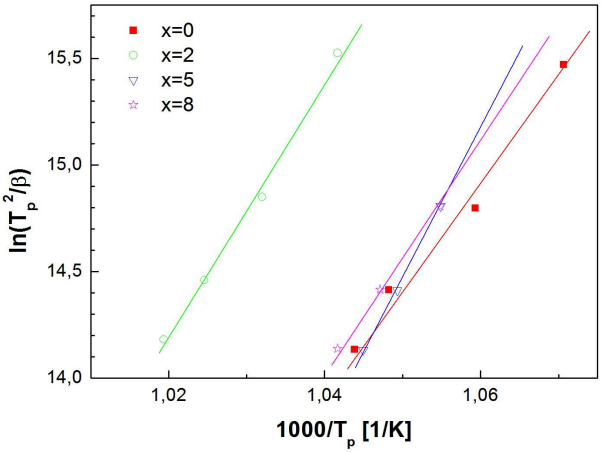

Fig. 2. Kissinger plots for crystallization of ribbons of $Pr_9Fe_{50+x}Co_{13}Zr_1Nb_4B_{23-x}$ ($x = 0$, 2, 5, 8) alloys.

TABLE II

Melting temperatures (T_m), liquidus temperatures (T_l) and GFA parameters ($T_{rg} = T_g/T_l$ — reduced glass transition temperature and $\gamma = T_x/(T_g + T_l)$) determined for amorphous ribbons of $Pr_9Fe_{50+x}Co_{13}Zr_1Nb_4B_{23-x}$ ($x = 0$, 2, 5, 8) alloys.

x [at.%]	T_m [K]	T_l [K]	T_{rg}	γ
0	1346	1412	0.62	0.407
2	1348	1412	0.59	0.425
5	1347	1411	0.60	0.420
8	1346	1415	0.59	0.420

The example XRD scans measured for ribbons of $x = 2$ alloy, annealed at various temperatures, with identified crystalline phases are presented in Fig. 3.

For ribbon annealed at 923 K except for reflexes coming from crystalline phases a pronounced bump characteristic of the amorphous phase was observed. The XRD traces have shown changes of peak intensities for samples annealed at higher temperatures. The XRD scans were subjected to the Rietveld refinement using Topas 4.2 software in order to determine the fractions of constituent phases formed during annealing as well as their crystallite sizes. The studies show presence of hard magnetic $Pr_2(Fe, Co)_{14}B$ and paramagnetic $Pr_{1+\varepsilon}Fe_4B_4$ phases for specimens of all investigated compositions. However, weight fractions of these phases change significantly with the alloy composition and annealing temperature. Furthermore, a presence of α-Fe phase was observed for rib-

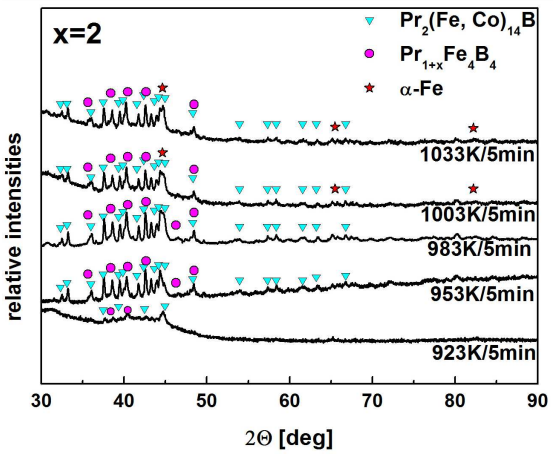

Fig. 3. The XRD scans measured for ribbons of $Pr_9Fe_{52}Co_{13}Zr_1Nb_4B_{21}$ alloy, annealed at various temperatures, with marked crystalline phases.

bons annealed at temperatures higher than 953 K. This is accompanied by decrease of the weight fraction of the hard magnetic phase that reaches ≈ 80 wt% for $x = 5$ and $x = 8$ alloys and decreases to ≈ 60 wt% when crystallization of α-Fe occurs. For the $x = 0$ and $x = 2$ alloys the fraction of $Pr_{1+\varepsilon}Fe_4B_4$ reaches up to 50 wt% depending on the annealing temperature, while for $x = 5$ and $x = 8$ alloys it decreases to ≈ 10 wt% for all annealing temperatures. The crystallite sizes were determined taking into account the instrument contribution to the diffraction lines broadening. The instrument characteristic was specified using XRD studies of LaB_6 standard sample followed by the Rietveld analysis. For all investigated ribbons ≈ 10 nm diameter crystallites of the $Pr_{1+\varepsilon}Fe_4B_4$ phase and ≈ 40 nm of the $Pr_2(Fe, Co)_{14}B$ phase were calculated by the whole pattern fitting method.

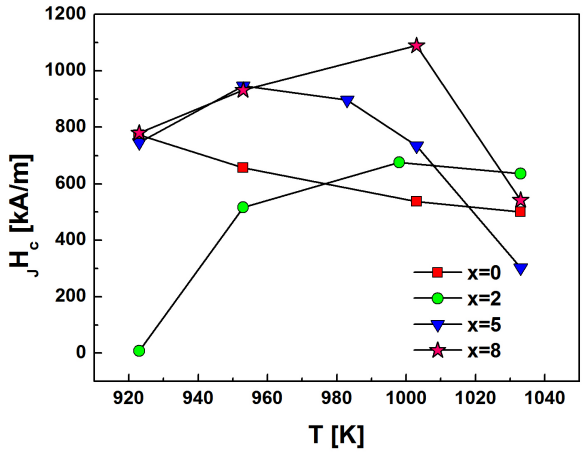

Fig. 4. Dependences of coercivity of $Pr_9Fe_{50+x}Co_{13}Zr_1Nb_4B_{23-x}$ alloy ribbons on the annealing temperature.

Dependences of coercivity field $_JH_C$ on the annealing temperature T are shown in Fig. 4. For all studied specimens, a change of magnetic properties was shown. The largest $_JH_C$ values were measured for $x = 5$ and $x = 8$ alloys. Its decrease for samples annealed at 1003 K and higher temperatures might be related to lower weight fraction of the hard magnetic phase and formation of the α-Fe. Lower fractions of the $Pr_2(Fe, Co)_{14}B$ phase accompanied by high amount of the $Pr_{1+\varepsilon}Fe_4B_4$ phase for $x = 0$ and $x = 2$ alloys resulted in lower maximum values of $_JH_C$. $(\boldsymbol{BH})_{\max}$ depends on alloy composition and annealing temperature and it reaches 65.4 kJ/m^3 for $x = 8$ alloy ribbons annealed at 1003 K.

4. Conclusions

Thermal studies of $Pr_9Fe_{50+x}Co_{13}Zr_1Nb_4B_{23-x}$ ($x = 0, 2, 5, 8$) alloy ribbons have shown large ΔT_x in all cases. Furthermore, it was shown that crystallization proceeds by simultaneous precipitation of two crystalline phases — the hard magnetic $Pr_2(Fe,Co)_{14}B$ and paramagnetic $Pr_{1+\varepsilon}Fe_4B_4$. Large values of E_a (especially for the $x = 2$ alloy) indicate high stability of the amorphous phase. XRD analysis has shown that annealing causes formation of ≈ 10 nm size crystallites of the $Pr_{1+\varepsilon}Fe_4B_4$ and ≈ 40 nm crystallites of $Pr_2(Fe, Co)_{14}B$ for all alloys composition and annealing temperatures. Increase of the annealing temperature causes formation of the α-Fe phase accompanied by decrease of the weight fraction of the $Pr_2(Fe,Co)_{14}B$ phase. It has also an outcome in the decrease of the coercivity of the samples.

References

[1] P. Pawlik, H.A. Davies, W. Kaszuwara, J.J. Wysłocki, *J. Magn. Magn. Mater.* **290-291**, 1243 (2005).

[2] S. Hirosawa, H. Kanekiyo, Y. Shigemoto, T. Miyoshi, in: *Proc. 18th Int. Workshop on High Performance Magnets and their Applications, Annecy (France)*, 2004, p. 655.

[3] P. Pawlik, K. Pawlik, H.A. Davies, J.J. Wysłocki, W. Kaszuwara, *J. Phys. Conf. Series* **144**, 012060 (2009).

[4] H.W. Chang, M.F. Shih, C.W. Chang, C.C. Hsieh, Y.T. Cheng, W.C. Chang, A.C. Sun, Y.D. Yao, *Scr. Mater.* **59**, 227 (2008).

[5] J. Zhang, K.Y. Lim, Y.P. Feng, Y. Li, *Scr. Mater.* **56**, 943 (2007).

[6] K. Pawlik, P. Pawlik, J.J. Wysłocki, *Acta Phys. Pol. A* **118**, 900 (2010).

[7] P. Pawlik, H.A. Davies, *Scr. Mater.* **49**, 755 (2003).

[8] A. Inoue, T. Zhang, T. Masumoto, *J. Non-Cryst. Solids* **156-158**, 473 (1993).